Cite this article
Soechiarto ED, Wűthrich D and Chanson H (2022)
Compression waves in semi-circular channel.
Proceedings of the Institution of Civil Engineers – Water Management **175(5)**: 247–256,
https://doi.org/10.1680/jwama.21.00022

Research Article
Paper 2100022
Received 26/05/2021;
Accepted 27/05/2021;
Published online 04/03/2022

Water Management

ice Publishing

Compression waves in semi-circular channel

Emelia Dara Soechiarto BEng
Civil Engineer, School of Civil Engineering, The University of Queensland, Brisbane, Australia

Davide Wűthrich PhD
Assistant Professor, Department of Hydraulic Engineering, Delft University of Technology, CN Delft, The Netherlands; formerly School of Civil Engineering, The University of Queensland, Brisbane, Australia (Orcid:0000-0003-1974-3560)

Hubert Chanson PhD, DEng
Professor, School of Civil Engineering, The University of Queensland, Brisbane, Australia (Orcid:0000-0002-2016-9650) (corresponding author: h.chanson@uq.edu.au)

Partially filled pipe flows are commonly observed in urban hydraulics, sewers and road crossings. The occurrence of a compression wave in the confined space may result from flash flooding, transient operation or accidental blockage, inducing explosive conditions. In this study, the propagation of a compression wave was studied in a relatively large laboratory flume of semi-circular cross-section. The unsteady flow properties were recorded to understand how the circular cross-sectional shape impacted the surging water propagation. Both free-surface and velocity data indicated a marked impact of the compression wave passage, with large instantaneous fluctuations comparable to and sometimes larger than observations of compression waves in rectangular channels.

Keywords: hydraulics & hydrodynamics/sewers & drains/waterways & canals

Notation

A	cross-sectional area
B	free-surface width
D	internal pipe diameter
D_H	hydraulic diameter
d	water depth measured above the lowest invert elevation
d_1	initial steady flow depth measured above the lowest invert elevation
d_c	critical flow depth
Fr	Froude number of compression wave
f	Darcy–Weisbach friction factor
f_{skin}	dimensionless skin friction boundary shear stress expressed in the form of a friction factor
g	gravitational acceleration
h	Tainter gate opening after closure
P_w	wetted perimeter
Q	initial steady flow discharge
R	internal pipe radius (= $D/2$)
Re	Reynolds number defined in terms of the hydraulic diameter (= $\rho V D_H/\mu$)
t	time
U	compression wave celerity
V	velocity
V_1	initial steady flow cross-sectional averaged velocity
V_x	instantaneous longitudinal velocity component
V_y	instantaneous transverse velocity component
v_x	instantaneous longitudinal velocity fluctuation
x	longitudinal coordinate positive downstream
y	transverse coordinate
z	vertical coordinate positive upwards
z_o	invert elevation (m)
α	kinetic energy correction coefficient
β	momentum correction coefficient
μ	dynamic viscosity of water
ρ	density of water

1. Introduction

Open-channel flows in circular conduits commonly occur in culverts, sewers, stormwater drains and hydropower tunnels (Hager, 1999; Sterling and Knight, 2000) (Figure 1(a)). Similarly, semi-circular flumes are common in water supply and irrigation systems (Repogle and Chow, 1966). The circular shape is extremely simple, yet it is a difficult shape for open-channel flow analyses because the cross-sectional shape continually varies with increasing flow depth (Kazemipour, 1979; Sterling, 1998) (Figure 1(b)). The variation in free-surface width B, cross-section area A, wetted perimeter P_w and hydraulic diameter D_H with increasing water depth d, is shown in Figure 1(b), where R is the radius of the circular open-channel (Figure 1(c)).

During some transient conditions in open channels, a sudden rise in water level is called a compression wave (Favre, 1935; Treske, 1994). The surging waters may induce large transient turbulent stresses, linked to intense turbulent mixing and strong sedimentary transport (Furgerot *et al.*, 2016; Khezri and Chanson, 2012). In partially filled pipes, the propagation of a compression wave can further create explosive conditions, in particular when the free-surface flow quasi-instantly transitions into a pressurised pipe flow (Capart *et al.*, 1997; Pozos-Estrada *et al.*, 2015). Such an explosive transition was recorded in January 2020 in Belo Horizonte, Brazil, during a flash flood induced by heavy rains. The Arrudas River surged in its covered conduit and burst through the obvert, with geysers jetting out of manholes and road collapses. One-dimensional (1D) unsteady flows in storm sewers have been investigated in several studies, with a focus on the transition from free-surface flow to pressurised flow (e.g. Capart *et al.*, 1997; Cunge and Wegner, 1964; Song *et al.*, 1983). However, studies on transient turbulence during compression wave propagation in circular pipes have not yet been reported.

(a)

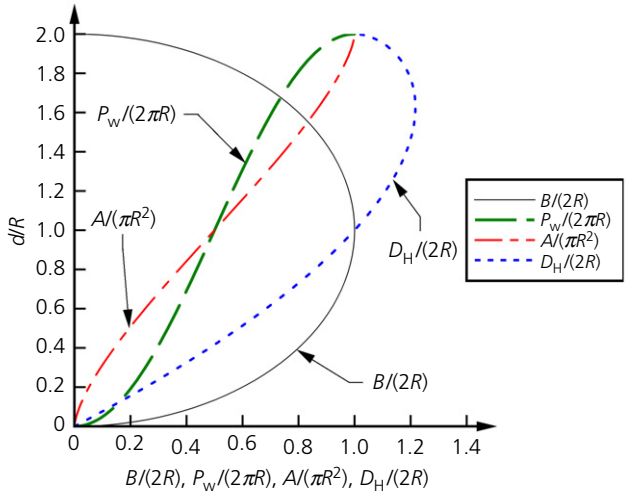

(b)

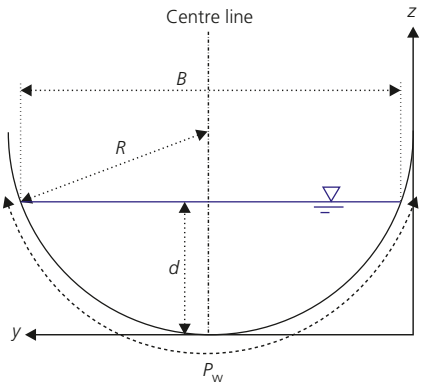

(c)

Figure 1. Circular conduits: (a) pipe culvert outlet in Brisbane on 9 February 2020; (b) dimensionless relationships between the free-surface width B, cross-section area A, wetted perimeter P_w, hydraulic diameter D_H and water depth d; (c) definition sketch

In this work, the unsteady turbulent characteristics of surging waters in a semi-circular channel were characterised through laboratory experiments in a relatively large flume (Figure 2). The aim was to gain some understanding on how a sudden change in cross-sectional shape in circular conduits may impact, or not, the compression wave propagation and transient characteristics.

2. Physical facility and metrology

The laboratory experiments were conducted in a semi-circular channel in the AEB hydraulic laboratory at the University of Queensland. The bed was horizontal for all the experiments. The test section was 13.25 m long, with a semi-circular PVC invert of 0.5 m diameter and vertical glass walls above (Figure 2). A smooth transition section was installed between $x = 0.11$ m and $x = 1.23$ m at the upstream end, while the semi-circular section ended with an abrupt drop and expansion into a 0.5 m wide rectangular section (x is the longitudinal coordinate measured from the upstream end of the flume).

In steady flows, the water elevations and longitudinal velocities were respectively measured with a pointer gauge and a Prandtl–Pitot tube of diameter 3.3 mm. During the compression wave experiments, water depth measurements were performed using five ultrasonic sensors (Microsonic Mic + 25) located along the channel centreline above the flume. The centreline velocities were recorded using an acoustic Doppler velocimeter (ADV) (Nortek Vectrino+) positioned at $x = 7.15$ m and $y = 0.25$ m for several vertical elevations. The ultrasonic sensors and ADV unit were sampled continuously, simultaneously and synchronously, within 1 ms, at 200 Hz for the full duration of each run. The velocimeters were positioned with a fine adjustment travelling mechanism connected to a Hafco digital scale unit, with an error on the vertical position $\Delta z < \pm 0.025$ mm. The error on the longitudinal and transverse position was $\Delta x < \pm 2$ mm and $\Delta y < 1$ mm respectively.

Compression waves were generated by the rapid closure of a semi-circular shaped Tainter gate located at $x = 14.0$ m. Closure of the gate took place in less than 0.3 s and had no impact on the compression wave propagation. Once generated, the compression wave advanced upstream against an initially steady free-surface flow (Figure 2). All recordings ended when the surging waters reached the upstream end of the flume. All the unsteady flow measurements were repeated 25 times and the ensemble statistics of the dataset were calculated. The flow conditions for the steady flow and compression wave experiments are summarised in Tables 1 and 2, respectively.

3. Steady flow characteristics

The steady flow properties in the semi-circular channel were measured for flow rates between 0.005 m^3/s and 0.080 m^3/s (Table 1). For all discharges, the flow was subcritical, that is $d > d_c$ (d_c is the critical depth and the flow depth (d) decreased with increasing longitudinal distance). In other words, the

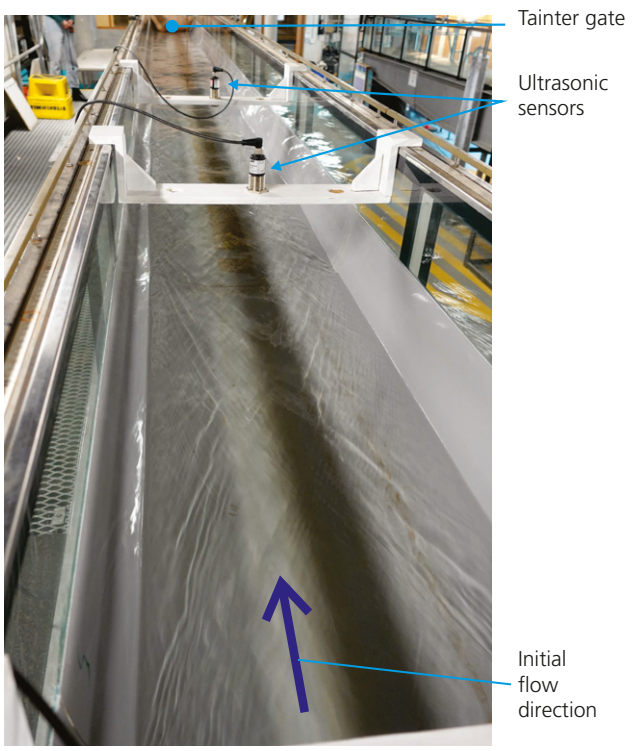

Figure 2. The experimental channel with $Q = 0.015$ m^3/s (looking downstream)

longitudinal free-surface data showed a H2 backwater profile for all discharges.

Velocity data from the semi-circular flume indicated low velocities in the close vicinity of the semi-circular wetted perimeter and significantly larger velocities in the bulk of the flow. Typical contour maps of the longitudinal velocity component (V_x) at two longitudinal distances ($x = 2.00$ m and $x = 7.15$ m) are presented in Figure 3. At $x = 2.00$ m, the velocity distributions were quasi-uniform, except next to the wetted perimeter, where some large velocity gradients were recorded next to the invert. Further downstream, at $x = 7.15$ m, the velocity profiles became fully developed, with the maximum longitudinal velocity observed next to the free surface on the channel centreline, while the velocity gradients next to the invert were large along the entire wetted perimeter. Further information on the velocity properties is summarised in Appendix 1, including the Boussinesq and Coriolis coefficients and the ratio of skin friction to total drag. Altogether, the water depth and velocity observations presented findings similar to and consistent with past steady flow measurements in semi-circular channels (Kazemipour, 1979; Repogle, 1964; Sterling, 1998).

The free-surface profiles were analysed to derive the Darcy–Weisbach friction factor (f) of the semi-circular channel based on energy considerations (i.e. using the best data fit between measured and calculated total head line slopes). The data obtained in this work are compared with previous datasets in Figure 4 (Chanson, 2020; Kazemipour, 1979; Sterling, 1998). Figure 4 also shows the Karman–Nikuradse formula for smooth turbulent boundary layer flows (Chanson, 2004; Liggett, 1994). Overall, the flow resistance in smooth semi-circular channels was close to, but slightly larger than, that in smooth turbulent flows (Figure 4). It is believed that this difference accounted for the turbulent dissipation by secondary motion induced by the circular cross-sectional shape.

4. Unsteady flow patterns

Detailed flow visualisations and free-surface measurements were performed for three flow rates, $Q = 0.015$ m^3/s, 0.035 m^3/s and 0.055 m^3/s, corresponding to an initial relative flow depth $d_1/D = 0.22$, 0.32 and 0.38, respectively. For each discharge, different patterns of compression waves were observed within a range of different openings (h) of the downstream Tainter gate, after closure (Figure 5). The compression wave properties were detailed at $x = 7.15$ m. Figures 5(a), 5(b) and 5(c) show typical photographic observations for different Froude numbers (from high to low). Details of the compression wave properties are provided in the figure caption, including the surge Froude number (Fr) at $x = 7.15$ m, defined as:

$$\text{Fr} = \frac{V_1 + U}{\sqrt{g \times A_1/B_1}} \quad (1)$$

where V_1 is the initially steady cross-sectional velocity, A_1 is the initial cross-section area, B_1 is the initial free-surface width and U is the celerity of the compression wave positive upstream. U was estimated from the ultrasonic sensor data.

Table 1. Properties at $x = 7.15$ m of steady flow conditions

Q: m^3/s	d: m	V: m/s	Re	A: m^2	B: m	P_w: m	f
0.080	0.228	0.917	1.2×10^5	0.08718	0.498	0.7413	0.016
0.055	0.191	0.798	0.93×10^5	0.06895	0.4858	0.6662	0.021
0.035	0.161	0.641	0.65×10^5	0.05463	0.4672	0.6034	0.0216
0.015	0.1085	0.477	3.5×10^4	0.0314	0.4122	0.4845	0.030
0.008	0.0875	0.347	2.1×10^4	0.02307	0.3799	0.4316	0.038
0.005	0.057	0.404	1.6×10^4	0.01238	0.3178	0.3444	0.0205

Table 2. Properties at $x = 7.15$ m of unsteady compression wave experiments

Q: m^3/s	d_1: m	V_1: m/s	U: m/s	Fr	h: m
0.055	0.191	0.797	0.803	1.567	0
			0.976	1.554	0.01
			0.901	1.488	0.02
			0.847	1.441	0.03
			0.837	1.432	0.04
			0.788	1.389	0.05
			0.746	1.352	0.06
			0.73	1.338	0.07
			0.666	1.282	0.08
0.035	0.161	0.64	0.909	1.496	0
			0.871	1.459	0.01
			0.81	1.401	0.02
			0.702	1.295	0.03
			0.691	1.285	0.04
			0.69	1.284	0.05
			0.636	1.232	0.06
			0.598	1.196	0.07
			0.564	1.163	0.08
0.015	0.109	0.477	0.68	1.384	0
			0.692	1.398	0.01
			0.651	1.350	0.02
			0.562	1.243	0.03
			0.519	1.192	0.04
			0.463	1.125	0.05
			0.417	1.069	0.06
			0.377	1.022	0.07
			0.359	1.000	0.08

For a Froude number barely larger than unity, the compression wave was very flat with a pseudo-2D undular free-surface profile, with some long wavelengths and small wave amplitudes. With an increasing Froude number, the undular compression wave became 3D, with the apparition of lateral cross-waves issuing from the sidewalls and intersecting about the channel centreline on the first wave crest (Figure 5(c)). The cross-waves continued to propagate downstream across the flume in a pseudo-diamond pattern, in plan view. The cross-wave onset indicated some form of flow separation at the sidewalls (Montes, 1986) associated with additional drag (Montes and Chanson, 1998). With a further increase in Froude number, the cross-waves became thicker upstream of the first crest and some breaking occurred at their intersection about the first wave crest, while some smaller cross-waves continued past the first crest (Figure 5(b)). The free-surface pattern was 3D with some small secondary waves behind the breaking region. At large Froude numbers, the breaking roller was quasi-2D, extending over the whole free-surface width (Figure 5(a)). The secondary waves disappeared and the roller was very energetic.

The unsteady patterns of the compression wave were systematically observed across all initial flow conditions, although, at low initial flow rates (i.e. $d_1/D < 0.25$), the arrival of the compression wave was associated with a significant change in cross-sectional shape. The thresholds between patterns differed depending on the initial relative flow depth (d_1/D). For the present experiments, the different compression wave states are shown in Figure 6, where the transition Froude number (Fr) is presented as a function of d_1/D. For larger initial discharges (i.e. $d_1/D > 0.35$), the compression wave tended to show more 2D patterns, similar to those observed during the propagation of compression waves in rectangular channels (Hornung *et al.*, 1995; Leng and Chanson, 2017).

Free-surface measurements were conducted non-intrusively at several longitudinal positions along the channel centreline using the ultrasonic sensors. An ultrasonic sensor is shown in Figure 5(c) above the surge front. Typical ensemble statistical results are presented in Figure 7 for a breaking surge. In Figure 7, both datasets were recorded with the same initial conditions ($Q = 0.035$ m^3/s, $d_1 = 0.161$ m). In the graph, the blue lines (Fr = 1.5) correspond to complete gate closure and stoppage of the flow. The surge was strong and travelling upstream at a celerity of $U = 0.91$ m/s. In contrast, the red lines (Fr = 1.28) relate to partial gate closure, resulting in a slower surge celerity ($U = 0.69$ m/s). Thus, the water surface surge time was earlier for Fr = 1.5. In Figure 7, time (t) is measured from the gate closure, the left-hand axis shows the dimensionless ensemble median depth (d_{50}/d_1) and the right-hand axis shows the difference in quartiles ($(d_{75}–d_{25})/d_1$), which characterised the instantaneous free-surface fluctuations (subscript 1 indicates initial flow conditions, 25 indicates the first quartile, 50 is the median and 75 is the third quartile). For all experiments and all types of surge, the median depth presented a sudden rise in free-surface elevation during the passage of the compression wave. The compression wave passage induced a sharp increase in water surface fluctuations (Figure 7). With undular surges, the median depth data showed a pseudo-periodic nature of the secondary undulations, as well as of the free-surface fluctuations (Figure 7, Fr = 1.28 (red lines)). The trends observed in this study were qualitatively comparable to observations in rectangular channels (Leng and Chanson, 2017), although the current free-surface data highlighted some more complicated patterns, often with larger free-surface fluctuations, after the passage of the compression wave front in the semi-circular channel.

The propagation of a compression wave may be solved using 1D unsteady open-channel flow equations called the Saint-Venant equations (SVE). Two approaches were tested in this work: (*a*) the method of characteristics based on simple wave approximation (Chanson, 2004; Henderson, 1966; Montes, 1998) and (*b*) numerical integration using the Hartree method (Courant *et al.*, 1952; Montes, 1998). The 1D solution was integrated from $x = 14$ m using the measured initial flow conditions and new discharge after closure of the Tainter gate for the downstream boundary condition. Both models produced very close results as the no-friction assumption in the simple wave solution was consistent with the hydraulically smooth flume.

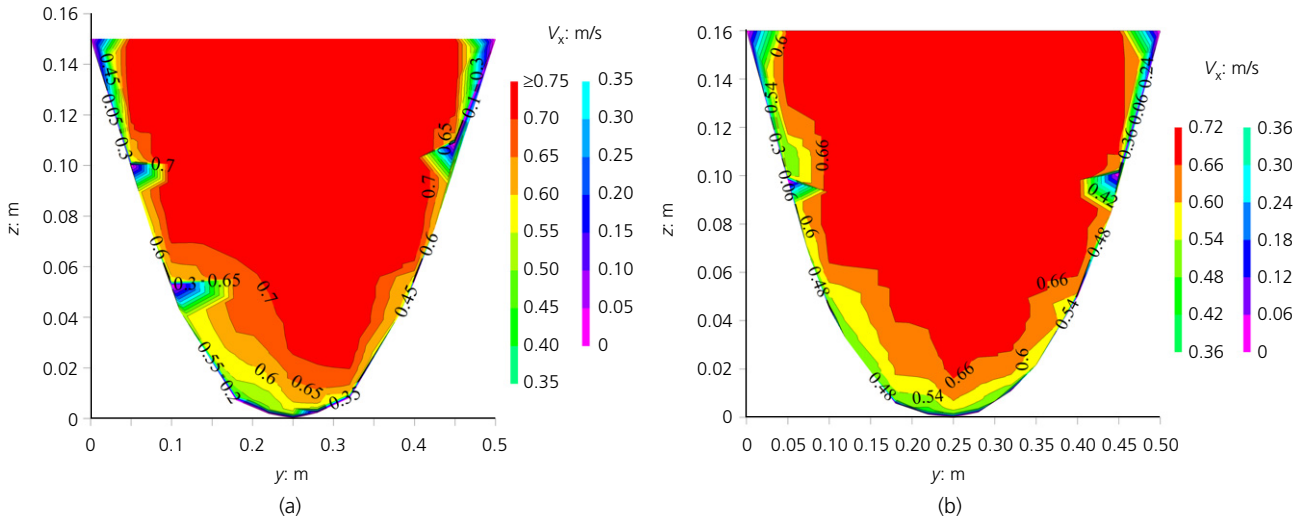

Figure 3. Contour maps of longitudinal velocity in semi-circular channel with a horizontal bed ($D = 0.50$ m, $Q = 0.035$ m^3/s) at: (a) $x = 2.00$ m; (b) $x = 7.15$ m

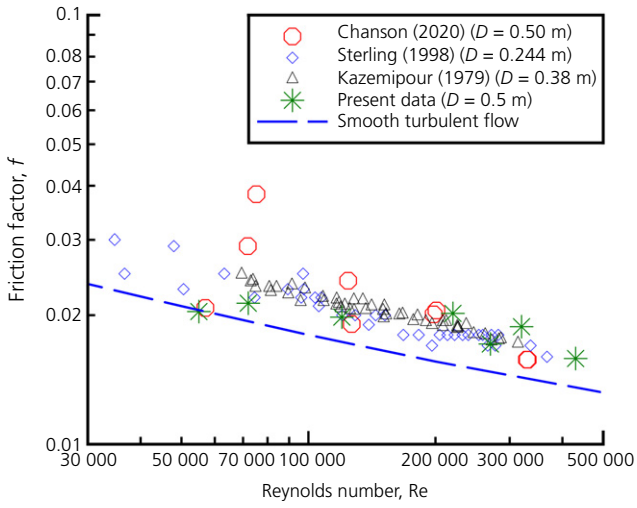

Figure 4. Flow resistance in smooth semi-circular channels: Darcy–Weisbach friction factor as a function of the Reynolds number. Comparison of current and previous datasets (Chanson, 2020; Kazemipour, 1979; Sterling, 1998) and smooth turbulent flow (Karman-Nikuradse formula)

A comparison of the physical observations and the unsteady flow model showed some agreement in terms of the compression wave celerity and height at $x = 7.15$ m. However, the 1D model significantly underestimated the arrival time of the compression wave. This is illustrated in Figure 8, which shows the measured median water depth and the computer-generated depth. The difference is believed to be linked to the compression wave generation process and associated turbulent motion. The unsteady flow model assumed a quasi-instantaneous surge generation, within the physical gate closure time of less than 0.3 s, but the generation of the physical compression wave was a much more complicated and slower 3D physical turbulent process (Leng, 2018; Sun *et al.*, 2016). The sudden gate closure induced a water pile-up against the upstream side of the gate, with an overturning motion, followed by a plunging and breaking mechanism after the free surface overturned, leading to the generation of a breaking roller (Leng, 2018: pp. 105–106, Lubin *et al.*, 2010: p. 596; Sun *et al.*, 2016: pp. 91–93). The roller formation lasted a few seconds before a stable compression wave formed and propagated upstream in a relatively quasi-steady motion. The entire generation process was previously documented though physical and numerical computational fluid dynamics data, for a similar surge generation process with sudden Tainter gate closure (Lubin *et al.*, 2010; Reichstetter, 2011; Sun *et al.*, 2016). All previous experimental studies showed a relatively slow generation process. For example, in a 12 m long and 0.15 m wide rectangular channel, Reichstetter (2011) observed 'a difference of 7.8 s between the arrivals of the surge front of the simple wave method compared to the physical data' (p. 48), while Sun *et al.* (2016) noted 'the generation of the positive surge was a slower process' (p. 93) in a similar flume.

5. Unsteady velocity data

The upstream propagation of the compression wave caused a sudden flow deceleration as the surge advanced past the velocimeter sampling volume. This was followed by large fluctuations of all velocity components, after a short time lag. Figure 9 shows a typical dimensionless time evolution of ensemble median velocity (V_{50}) components and instantaneous velocity fluctuation ($V_{75} - V_{25}$), defined as the difference between the third and first quartile. For a normal distribution of the dataset about its mean value, the difference between third and first quartiles ($V_{75} - V_{25}$) would be equal to 1.3 times the standard deviation of the ensemble.

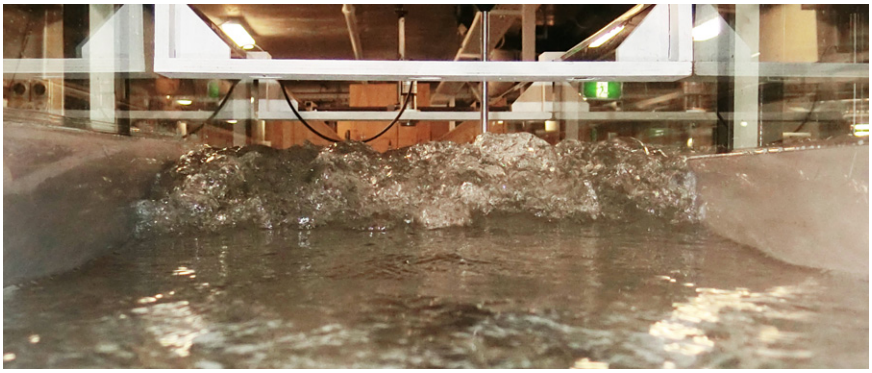

(a)

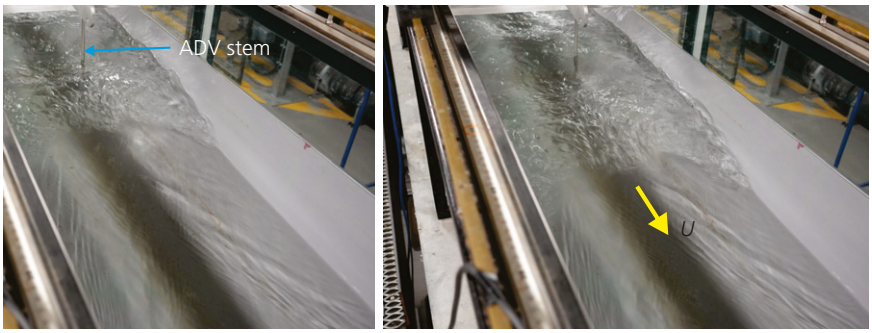

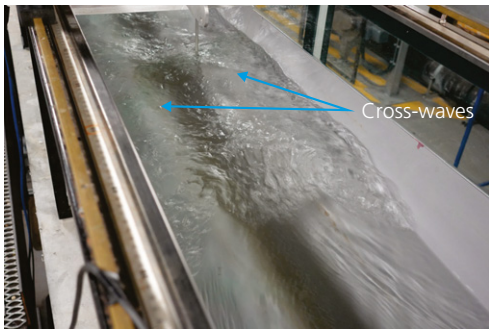

(b)

(c)

Figure 5. Basic observations of compression waves propagating in semi-circular channel ($D = 0.5$ m). (a) Two-dimensional breaking bore, looking downstream at incoming bore roller; $Q = 0.035$ m^3/s, $x = 7.15$ m, $d_1 = 0.161$ m, $U = 0.91$ m/s, Fr = 1.5. (b) Breaking bore with secondary undulations, with 0.3 s between each photograph; $Q = 0.015$ m^3/s, $x = 7.15$ m, $d_1 = 0.109$ m, $U = 0.68$ m/s, Fr = 1.38. (c) Undular surge with relatively weak cross-waves intersecting on the channel centreline about the first wave crest; $Q = 0.055$ m^3/s, $x = 7.15$ m, $d_1 = 0.191$ m, $U = 0.67$ m/s, Fr = 1.28 (left, three-quarter view; right: looking downstream at incoming compression wave)

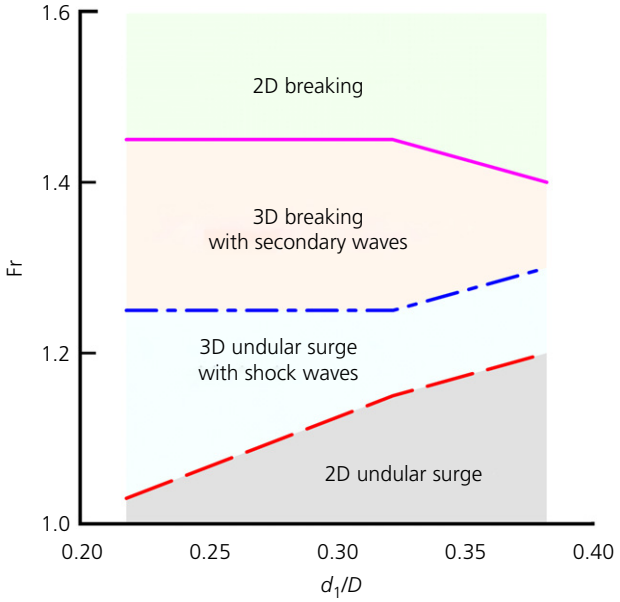

Figure 6. Dimensionless chart of the different compression wave states in a semi-circular channel: transition Froude number (Fr) as a function of initial relative depth (d_1/D)

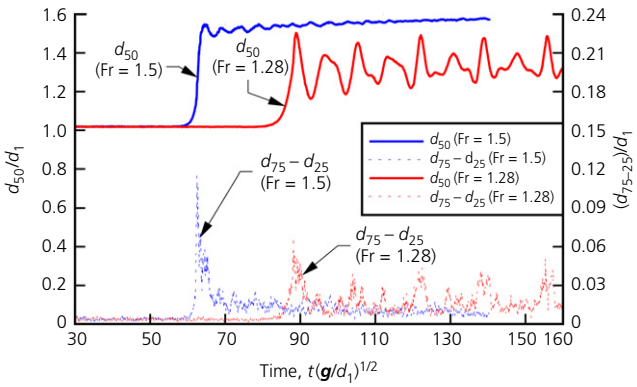

Figure 7. Dimensionless time variations of ensemble median water elevation d_{50} and quartile difference ($d_{75} - d_{25}$) of compression waves propagating upstream in semi-circular channel for two flow conditions. The blue lines are for Fr = 1.5 ($h = 0$), $Q = 0.035$ m^3/s, $x = 7.15$ m, $d_1 = 0.161$ m and $U = 0.91$ m/s (breaking bore). The red lines are for $Q = 0.035$ m^3/s, $x = 7.15$ m, $d_1 = 0.161$ m, Fr = 1.28 ($h = 0.050$ m) and $U = 0.69$ m/s (undular bore)

The longitudinal velocity data showed, at all elevations and for all discharges, a sharp deceleration with the passage of the compression wave. Figure 9(a) shows a typical example. Furthermore, the transverse and vertical velocity data exhibited some sharp fluctuations between the wave passage. Figure 9(b) shows a typical transverse velocity dataset. For all the velocity components, large instantaneous velocity fluctuations were observed during and shortly after the compression wave (Figure 9). In the present study, data recording was stopped when the compression wave reached the upstream end of the channel, to prevent any reflection effect. Thus, the velocity recoding was time-limited and any long-lasting effect observed in the field (e.g. Chanson *et al.*, 2011; Leng *et al.*, 2018) could not be documented.

Although the current measurements were conducted on the channel centreline, the arrival of the compression wave induced a 3D transient response of the velocity field. The response of the flow field to the surge may be analysed as an impulse problem (Kiri *et al.*, 2020; Lighthill, 1978). Theoretical considerations would predict large transverse velocities, on both sides, in the shallow-water sections, with an unsteady secondary motion and flow recirculation next to the sides (Figure 10). Figure 10 shows a solution of the impulse forcing imposed by a sudden longitudinal pressure gradient associated with the passage of a compression wave front in the semi-circular invert profile, with $d_1/D = 0.32$. The invert profile and the initial water depth are also shown in Figure 10. The transverse distribution of the depth-averaged longitudinal velocity was found to be related to the depth distribution, with recirculation in shallow waters (Figure 10). With such a short-lived transient process, the flow pattern would be consistent with the flow separation observed at the inception of cross-waves ahead of the first wave crest.

The Reynolds stress tensor was calculated for the data ensemble. Some typical data are presented in Figure 11 in terms of the normal turbulent stress ($v_x \times v_x$). Figure 11 shows the dimensionless time-variation of the instantaneous median and third quartile of the data ensemble, the latter characterising the instantaneous fluctuation in normal stress. At all elevations and for all flow rates, the turbulent stress data presented a marked increase in instantaneous median Reynolds stress and shear stress fluctuations during the passage of the compression wave and shortly after (Figure 11).

6. Conclusion

The propagation of compression waves in semi-circular channels is a complicated, often 3D, transient process. Detailed unsteady experiments in a large laboratory facility enables a combination of visual, free-surface and velocity measurements in a semi-circular channel. The free-surface observations indicated some complicated 3D features, with cross-waves and surface breaking for a range of Froude numbers. At a higher Froude number, the compression wave was quasi-2D with a breaking roller expanding across the entire channel width. The ensemble statistics of the free-surface and velocity measurements demonstrated the marked impacts of the passage of the compression wave. These included a sharp increase in water elevation and streamwise deceleration. The former may explain the explosive incidents reported in some urban waterways. Further seminal features were some large transient instantaneous fluctuations in terms of water depth, velocity components and Reynolds stresses.

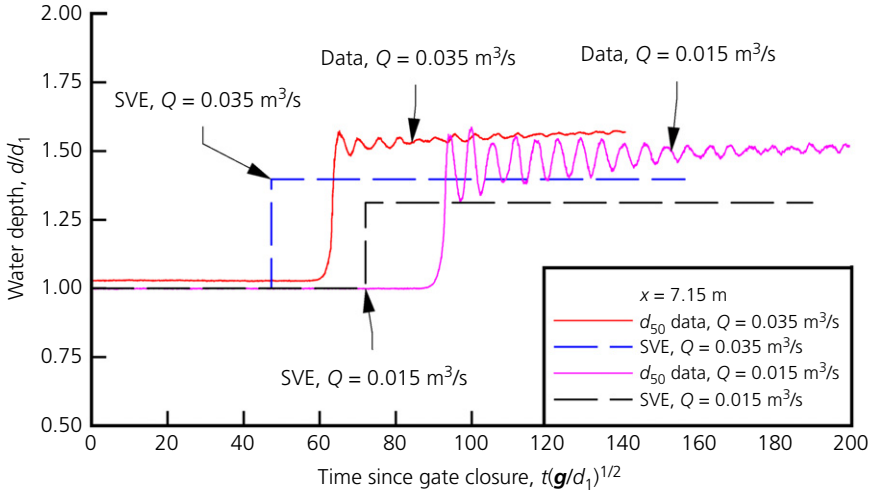

Figure 8. Dimensionless time variations of water elevation during compression wave propagation in a semi-circular channel: comparison between present experimental data (ensemble median of 25 repeats) and unsteady flow model based on the SVE for $Q = 0.035$ m³/s and $Q = 0.015$ m³/s

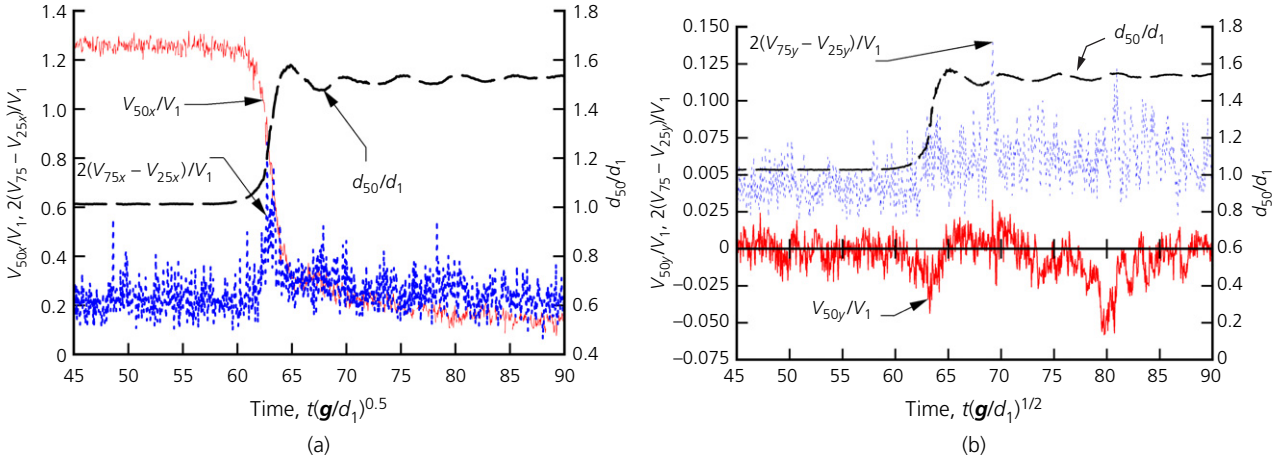

Figure 9. Dimensionless time variations of ensemble median longitudinal velocity (V_x) and transverse velocity (V_y), and quartile differences, during upstream propagation of compression wave in the semi-circular channel ($Q = 0.035$ m³/s, $x = 7.15$ m, $d_1 = 0.161$ m, $V_1 = 0.64$ m/s, $U = 0.70$ m/s, Fr = 1.44, $z = 0.140$ m): (a) V_x; (b) V_y

Further analyses hinted that a semi-circular channel shape tends to induce larger instantaneous fluctuations than the observations of positive surges in rectangular channels. Future research could include unsteady velocity measurements across the whole cross-section in order to characterise sidewall effects, including recirculation and secondary currents.

Acknowledgements

The authors are grateful for the technical assistance of Jason Van Der Gevel and Stewart Matthews (The University of Queensland, Australia) and the financial assistance of the School of Civil Engineering at The University of Queensland. HC thanks Dr Daniel Valero for sharing information on the Arrudas River incident.

Appendix 1. Key summary of velocity properties in semi-circular channel (present data)

Detailed steady flow measurements were conducted at two locations ($x = 2.00$ m and 7.15 m) in a semi-circular channel. The velocity data were analysed to derive the momentum correction coefficient β (or the Boussinesq coefficient) and the kinetic energy correction coefficient α (or the Coriolis coefficient). The skin friction boundary shear stress was recorded along the entire

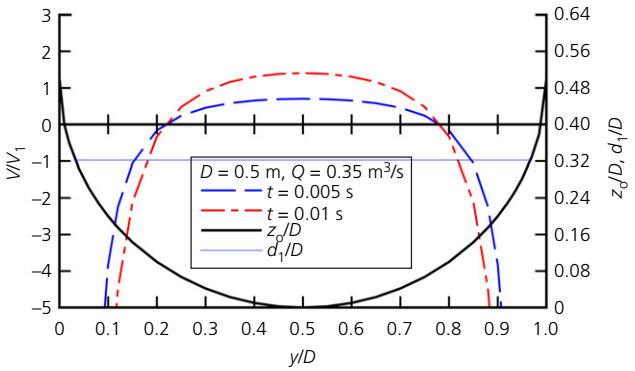

Figure 10. Transverse distribution of dimensionless longitudinal velocity (V/V_1) for impulse forcing imposed by a longitudinal pressure gradient during the passage of a compression wave in a semi-circular channel with $d_1/D = 0.32$

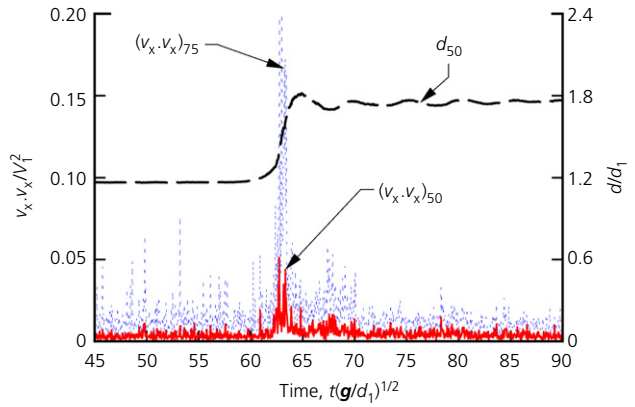

Figure 11. Dimensionless time variations of ensemble median normal stress ($v_x{\cdot}v_x$) and third quartile during the upstream propagation of compression wave in semi-circular channel ($Q = 0.035$ m^3/s, $x = 7.15$ m, $d_1 = 0.161$ m, $V_1 = 0.64$ m/s, $V_1 = 0.64$ m/s, $U = 0.70$ m/s, Fr = 1.44, $z = 0.140$ m)

wetted perimeter, using a Prandtl–Pitot tube acting as a Preston tube, based on detailed calibration of the tube by Cabonce *et al.* (2019). The data were then integrated, yielding the relative skin friction (f_{skin}/f). The data are summarised in Table 3.

Table 3. Steady flow measurements at $x = 2.00$ m and 7.15 m

	$Q = 0.035$ m^3/s		$Q = 0.08$ m^3/s	
	$x = 2.00$ m	$x = 7.15$ m	$x = 2.00$ m	$x = 7.15$ m
V_{mean}: m/s	0.656	0.709	0.798	0.884
d: m	0.168	0.160	0.236	0.230
A: m^2	0.0579	0.0542	0.091	0.088
P_w: m	0.618	0.601	0.758	0.745
β	1.051	1.096	1.061	1.072
α	1.128	1.169	1.112	1.105
f_{skin}/f	0.781	0.639	0.897	0.602

REFERENCES

Cabonce J, Fernando R, Wang H and Chanson H (2019) Using small triangular baffles to facilitate upstream fish passage in standard box culverts. *Environmental Fluid Mechanics* **19(1)**: 157–179, 10.1007/s10652-018-9604-x.

Capart H, Sillen X and Zech Y (1997) Numerical and experimental water transients in sewer pipes. *Journal of Hydraulic Research* **35(5)**: 659–672.

Chanson H (2004) *Environmental Hydraulics of Open Channel Flows.* Elsevier–Butterworth-Heinemann, Oxford, UK.

Chanson H (2020) Low velocity zone in smooth pipe culvert with and without streamwise rib for fish passage. *Journal of Hydraulic Engineering* **146(9)**: 04020059, https://doi.org/10.1061/(ASCE)HY.1943-7900.0001789.

Chanson H, Reungoat D, Simon B and Lubin P (2011) High-frequency turbulence and suspended sediment concentration measurements in the Garonne River tidal bore. *Estuarine Coastal and Shelf Science* **95(2–3)**: 298–306, https://doi.org/10.1016/j.ecss.2011.09.012.

Courant R, Isaacson E and Rees M (1952) On the solution of nonlinear hyperbolic differential equations by finite differences. *Communications on Pure and Applied Mathematics* **5(3)**: 243–255.

Cunge JA and Wegner M (1964) Intégration numérique des equations d'ecoulement de barré de Saint Venant par une schéma implicite de différences finies. *La Houille Blanche* **50(1)**: 33–39 (in French).

Favre H (1935) *Etude Théorique et Expérimentale des Ondes de Translation Dans les Canaux Découverts.* Dunod, Paris, France (in French).

Furgerot L, Mouaze D, Tessier B *et al.* (2016) Sediment transport induced by tidal bores. an estimation from suspended matter measurements in the Sée River (Mont-Saint-Michel Bay, northwestern France). *Comptes Rendus Géoscience* **348**: 432–441, 10.1016/j.crte.2015.09.004.

Hager WH (1999) *Wastewater Hydraulics.* Springer-Verlag, Berlin, Germany.

Henderson FM (1966) *Open Channel Flow.* MacMillan Company, New York, NY, USA.

Hornung HG, Willert C and Turner S (1995) The flow field downstream of a hydraulic jump. *Journal of Fluid Mechanics* **287**: 299–316.

Kazemipour AK (1979) *Cross-sectional Shape Effects on Resistance to Uniform Flow in Open Channels and Non-Circular Closed Conduits.* PhD thesis, The University of Queensland, Department of Civil Engineering, Brisbane, Australia.

Khezri N and Chanson H (2012) Sediment inception under breaking tidal bores. *Mechanics Research Communications* **41**: 49–53, https://doi.org/10.1016/j.mechrescom.2012.02.010.

Kiri U, Leng X and Chanson H (2020) Transient secondary currents behind a compression wave in an irregular channel. *Environmental Fluid Mechanics* **20(4)**: 1053–1073, https://doi.org/10.1007/s10652-020-09740-y.

Leng X (2018) *A Study of Turbulence: The Unsteady Propagation of Bores and Surges.* PhD thesis, The University of Queensland, Brisbane, Australia, https://doi.org/10.14264/uql.2018.501.

Leng X and Chanson H (2017) Upstream propagation of surges and bores: free-surface observations. *Coastal Engineering Journal* **59(1)**: 1750003, https://doi.org/10.1142/S0578563417500036.

Leng X, Chanson H and Reungoat D (2018) Turbulence and turbulent flux events in tidal bores: case study of the undular tidal bore of the Garonne River. *Environmental Fluid Mechanics* **18(4)**: 807–828, https://doi.org/10.1007/s10652-017-9561-9.

Liggett JA (1994) *Fluid Mechanics.* McGraw-Hill, New York, NY, USA.

Lighthill J (1978) *Waves in Fluids.* Cambridge University Press, Cambridge, UK.

Lubin P, Chanson H and Glockner S (2010) Large eddy simulation of turbulence generated by a weak breaking tidal bore. *Environmental Fluid Mechanics* **10(5)**: 587–602, 10.1007/s10652-009-9165-0.

Montes JS (1986) A study of the undular jump profile. In *Proceedings of the 9th Australasian Fluid Mechanics Conference (AFMC), Auckland, New Zealand*. University of Auckland, School of Engineering (NZ), Auckland, New Zealand, pp. 148–151.

Montes JS (1998) *Hydraulics of Open Channel Flow*. ASCE, New York, NY, USA.

Montes JS and Chanson H (1998) Characteristics of undular hydraulic jumps. Results and calculations. *Journal of Hydraulic Engineering* **124(2)**: 192–205, https://doi.org/10.1061/(ASCE)0733-9429(1998)124:2(192).

Pozos-Estrada O, Pothof I, Fuentes-Mariles OA *et al.* (2015) Failure of a drainage tunnel caused by an entrapped air pocket. *Urban Water Journal* **12(6)**: 446–454, https://doi.org/10.1080/1573062X.2015.1041990.

Reichstetter M (2011) *Hydraulic Modelling of Unsteady Open Channel Flow: Physical and Analytical Validation of Numerical Models of Positive and Negative Surges*. MPhil thesis, The University of Queensland, Brisbane, Australia.

Repogle JA (1964) *Tractive-Force Distribution in Sewers and Channels*. PhD thesis, University of Illinois, Champaign, IL, USA.

Repogle JA and Chow VT (1966) Tractive-force distribution in open channels. *Journal of the Hydraulic Division* **92(HY2)**: 169–191.

Song CCS, Cardle JA and Leung KS (1983) Transient mixed-flow models for storm sewers. *Journal of Hydraulic Engineering* **109(11)**: 1487–1504.

Sterling M (1998) *A Study of Boundary Shear Stress, Flow Resistance and the Free Overfall in Open Channels with A Circular Cross Section*. PhD thesis, University of Birmingham, Birmingham, UK.

Sterling M and Knight DW (2000) Resistance and boundary shear in circular conduits with flat beds running part full. *Proceedings of the Institution of Civil Engineers – Water and Maritime Engineering* 142(4): 229–240, https://doi.org/10.1680/wame.2000.142.4.229.

Sun S, Leng X and Chanson H (2016) Rapid operation of a Tainter gate: generation process and initial upstream surge motion. *Environmental Fluid Mechanics* **16(1)**: 87–100, 10.1007/s10652-015-9414-3.

Treske A (1994) Undular bores (Favre-waves) in open channels – experimental studies. *Journal of Hydraulic Research* **32(3)**: 355–370.